Supporting Information

Hydrogenation and C-S bond activation pathways in thiophene and tetrahydrothiophene reactions on sulfur-passivated surfaces of Ru, Pt, and Re nanoparticles

Edwin Yik, David Hibbitts, Huamin Wang, and Enrique Iglesia

Department of Chemical and Biomolecular Engineering, University of California,
Berkeley, CA 94720, USA
Department of Chemical Engineering, University of Florida,
Gainesville, FL 32611, USA

S.1 S adatom Adsorption Energies from DFT Calculations

Table S.1-1: Relative potential energies (kJ mol^{-1}) for S adatom adsorption in various binding modes at 1/9 ML.

	Ru(0001)	*Re(0001)*	*Pt(111)*
three-fold fcc	8	7	0
three-fold hcp	0	0	15
atop	149	123	199

Table S.1-2: Relative potential energies (kJ mol^{-1}) for S adatom adsorption in various S–S distances and binding modes at 2/9 ML.

relative distance [a]		*Ru(0001)*	*Re(0001)*	*Pt(111)*
1	hcp	24	1	51
1	fcc	42	13	42
$\sqrt{7/3}$	mix	17	0	16
$\sqrt{3}$	hcp	0	1	30
$\sqrt{3}$	fcc	6	41	0

[a] distance between three-fold binding modes relative to the bulk M–M distance; does not account for S adatom relaxation which increases S–S distances for the close (1) values by 15-25%.

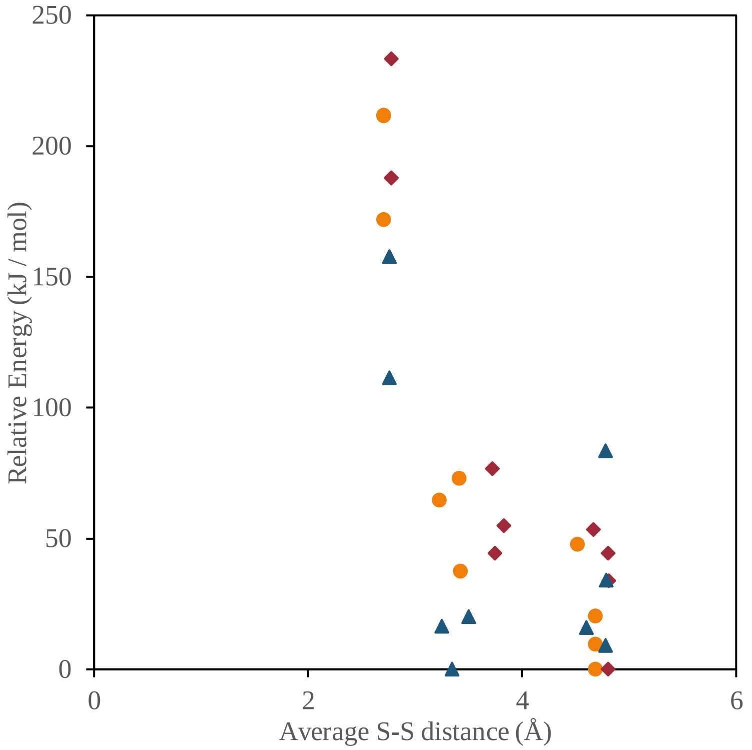

Figure S.1-1: Relative energies (kJ mol^{-1}) for various S adatom configurations at 3/9 ML for Ru(0001) (●), Re(0001) (▲), and Pt(111) (◆).

Table S.1-3: Differential adsorption enthalpies (kJ mol^{-1}), entropies (J mol^{-1} K^{-1}), and free energies (kJ mol^{-1}, 600 K, 1 bar) at various adatom coverages.

S adatom coverage	*Ru(0001)*			*Re(0001)*			*Pt(111)*		
ML	*H*	*S*	*G*	*H*	*S*	*G*	*H*	*S*	*G*
1/9	-203	-42	**-177**	-201	-42	**-175**	-125	-46	**-98**
2/9	-195	-42	**-170**	-187	-42	**-162**	-106	-45	**-79**
1/3	-192	-42	**-167**	-181	-48	**-152**	-84	-43	**-58**
4/9	-100	-50	**-70**	-146	-46	**-118**	41	-50	**71**
5/9	-46	-53	**-14**	-78	-49	**-48**			
2/3	45	-48	**74**	-27	-57	**7**			
7/9	172	-41	**196**	76	-53	**108**			
8/9	229	-26	**244**	108	-57	**143**			
1	210	-34	**231**	117	-57	**152**			

S.2 Sulfur atom adsorption on 201-atom Ru, Re, and Pt particles.

Prior work has indicated that periodic surface models, like those used here, can incorrectly predict sub-monolayer saturation for adsorbates such as CO* (on Ru) and NO* (on Rh). Therefore, cubo-octahedral 201-atom particle models of Ru, Re, and Pt were used to examine S adsorption. Sulfur atom adlayers on 201-atom Ru, Re, and Pt particles were generated by occupying all three-fold hcp sites on (111) terraces (3fh sites), all bridge sites on edges between (111) terraces (be11 sites), and four-fold hollow sites on (100) terraces (hol sites). These adlayers varied from 96–144 S atoms (0.79–1.18 ML, defined as S:M_{surf} ratio) and for each adlayer, a single S* was removed from the a 3fh site on the (111) terrace to determine a differential adsorption energy to assess the feasibility of S adlayers reaching such coverages.

Table S.2-1. Summary of high-coverage S* adsorption energies on single-crystal M(0001) or M(111) models and particle (M_{201}) models. (M = Ru, Re, or Pt).

Model	Binding Modes [b]	Covg. / ML	Avg. BE /kJ mol^{-1}	Diff. BE /kJ mol^{-1}
Ru(0001)	3fh	1.00	−7.9	+211.6
Ru_{201}	3fh	0.79	−117.1	+18.1
	3fh, be11	0.98	−87.2	+48.2
	3fh, be11, hol	1.18	−87.4	+68.1
Re(0001)	3fh	1.00	−57.0	+117.4
Re_{201}	3fh	0.79	−153.3	−23.7
	3fh, be11	0.98	−129.0	+52.3
	3fh, be11, hol	1.18	−138.7	u
Pt(111)	3fh	1.00	+18.0	+209.5
Pt_{201}	3fh	0.79	−24.6	u
	3fh, be11	0.98	u	u
	3fh, be11, hol	1.18	u	u

u: Indicates an unstable particle & adlayer as shown by significant restructuring during optimization. [b] Binding modes examined were three-fold hcp (3fh), bridge sites on edges between (111) facets (be11), and four-fold hollow sites on (100) facets (hol).

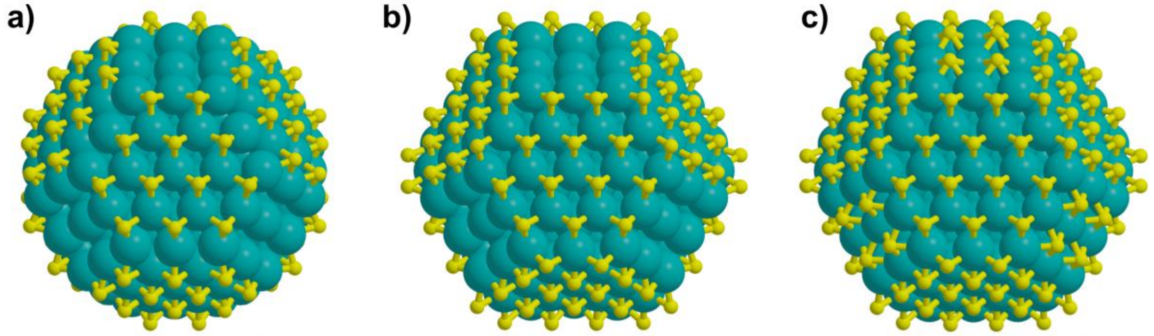

Ru$_{201}$: 3fh: 0.79 ML S
Avg. BE = −117
Diff. BE = +18

Ru$_{201}$: 3fh, be11: 0.98 ML S
Avg. BE = −87
Diff. BE = +48

Ru$_{201}$: 3fh, be11, hol: 1.18 ML S
Avg. BE = −87
Diff. BE = +68

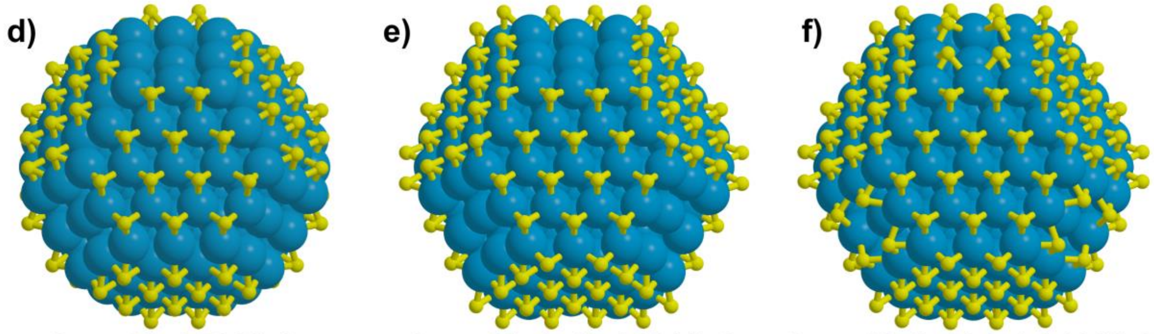

Re$_{201}$: 3fh: 0.79 ML S
Avg. BE = −153
Diff. BE = −24

Re$_{201}$: 3fh, be11: 0.98 ML S
Avg. BE = −129
Diff. BE = +52

Re$_{201}$: 3fh, be11, hol: 1.18 ML S
Avg. BE = −139

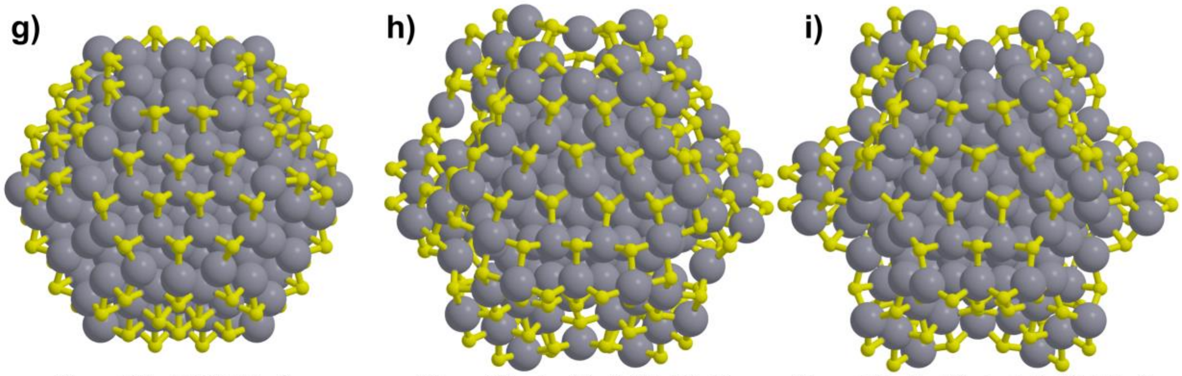

Pt$_{201}$: 3fh: 0.79 ML S
Avg. BE = −24

Pt$_{201}$: 3fh, be11: 0.98 ML S
Avg. BE = −42

Pt$_{201}$: 3fh, be11, hol: 1.18 ML S
Avg. BE = −32

Figure S.2-1: Sulfur adlayers on 201-atom particles of Ru (a-c), Re (d-f), and Pt (g-i). Adlayers were prepared by adding S at three-fold hcp sites on (111) terraces (3fh), at bridging sites on edges between (111) terraces (be11), and at four-fold hollow sites on (100) terraces (hol) to give surfaces of 0.79–1.18 ML S. Average S binding energies (Avg. BE, an average of all S) and a differential binding energy (Diff. BE, of a single S bound to a 3fh site on the (111) terrace) are given.

Sulfur adsorption energies (Table S.2-1) on Ru$_{201}$ particles indicate that adsorptions near 1 ML (0.79–1.18 ML) are more favorable on Ru$_{201}$ particles than at 1 ML on the Ru(0001) surface, consistent with prior studies which showed stronger binding on particle models than on periodic surface models [33-35, 38]. This is caused, in this case, primarily by the ability of the metal particle to laterally relax its surface (extending M–M bonds to weaken adsorbate–adsorbate repulsions). Differential sulfur adsorption energies, however, are endothermic on both the Ru(0001) surface (1 ML) and on Ru_{201} particle models (0.79–1.18 ML), indicating that these coverages are thermodynamically unfavorable, even at large H_2S/H_2 ratios.

On Re_{201} particles, as with Ru_{201}, adsorption energies indicate that adsorption is more favorable on the particle models than on Re(0001) surfaces. While adsorption remains slightly exothermic (Diff. BE = -24 kJ mol^{-1}) at 0.79 ML on Re_{201}, it is endothermic (Diff. BE = 52 kJ mol^{-1}) at 0.98 ML. The higher coverage adlayer (1.18 ML) significantly restructured upon removal of a S* atom from a 3fh site on the (111) terrace (used to compute Diff. BE), indicating the instability of that high coverage adlayer. These data, like those on Ru_{201}, indicate that coverages near 1 ML are unlikely, even at large H_2S/H_2 ratios (well above the range relevant to experimental HDS).

Finally, Pt_{201} particles showed significant instability (shown in Fig. S.2-1h and S.2-1i) at 0.98–1.18 ML, indicating that these surfaces are very unlikely to form. As a reminder, these are results of optimization calculations, not of annealing studies, and thus spontaneous S desorption (via S_2 or H_2S formation) is not possible in these calculations but is likely how the surface would alleviate these adlayer-adlayer repulsions. In the absence of reasonable desorption routes, the adlayer repulsion is alleviated through extreme restructuring of the metal surface. The extensive restructuring prevents calculation of differential adsorption energies, but the average adsorption energies indicate that these adlayers are very unlikely to form at experimental HDS conditions.

These data, in summary, indicate that S adlayers will have a mixture of refractory S adatoms, reversibly bound S adatoms, and empty sites (interstices) where reactions can occur because of the strong S–S repulsions within the adlayer. The coverage of these refractory S adlayers will vary amongst the metals of interest and will likely be higher for calculations based on particle models compared to surface models, but in no case will there be a fully S-covered particle at conditions of interest.

S.3 Sensitivity analysis of fitted parameters

Parameter values were obtained via non-linear regression of measured data to the functional form of rate equations for thiophene conversion on Ru/SiO_2 and Pt/SiO_2 (Eqs. 11 and 12, respectively) and reported in Table 2. The regression seeks to minimize residuals, at each condition *i*, between the model predicted ($r_{i,predicted}$) and measured rates ($r_{i,\ measured}$). The sum of square residuals, SSR, hence reflects a minimization of error, obtained upon enforcing the optimal parameter values, k_j (where $k_j = \alpha, \beta, \gamma, \eta$; Table 2):

$$Sum\ of\ Squares\ of\ Residuals\ (SSR) = \sum_i \left(r_{i,predicted} - r_{i,measured}\right)^2 \tag{S.3-1}$$

The sensitivity of these parameters can be probed by assessing the relative change in SSR upon imposing small perturbations (δ is between 0 and (0.2)·k_j) on a given k_j:

$$Relative\ Change\ in\ SSR = \frac{(SSR)|_{k_j \pm \delta} - (SSR)|_{k_j}}{(SSR)|_{k_j}} \tag{S.3-2}$$

The relative change in a given parameter is hence defined:

$$Relative\ Change\ in\ k_j = \frac{\pm\delta}{k_j} \tag{S.3-3}$$

A parameter is considered *sensitive* and hence relevant for describing measured data if the relative change in SSR (Eq. S.3-2) exceeds the relative change in the parameter k_j, over the range of ±δ from 0 to 0.2·k_j, i.e.,

$$\left|\frac{\partial(Relative\ Change\ in\ SSR)}{\partial(Relative\ Change\ in\ k_j)}\right| > 1 \tag{S.3-4}$$

Parameter values reported in Table 2 (α, γ, η for Ru and α, β, γ, η for Pt) are *sensitive*, as evident from Figures S.3-1 and S.3-2, for Ru and Pt, respectively.

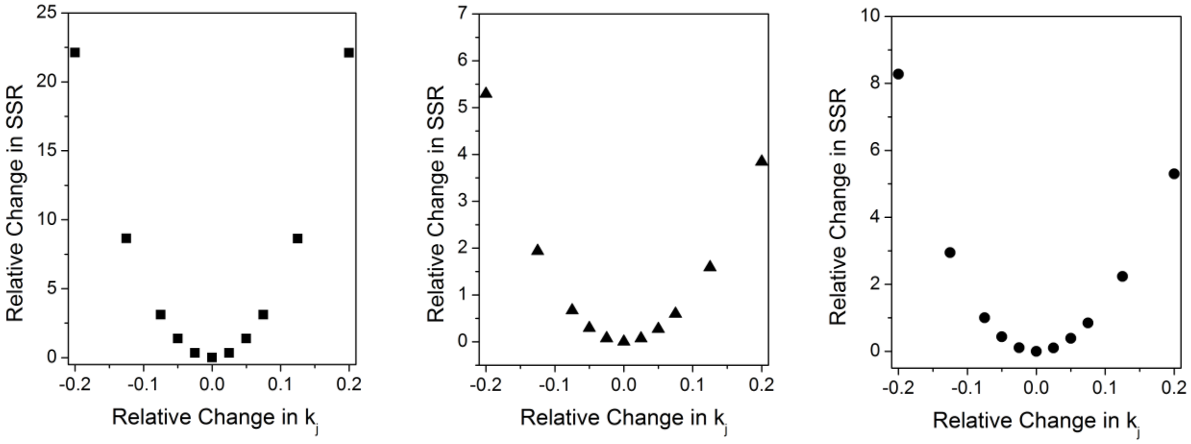

Figure S.3-1: Relative change in the sum of squared residuals (SSR) as a function of relative change (δ/k_j) in the optimal values (listed in Table 2) of the fitted rate (k_j) parameter for α (■), γ (▲), and η (●) on Ru/SiO$_2$.

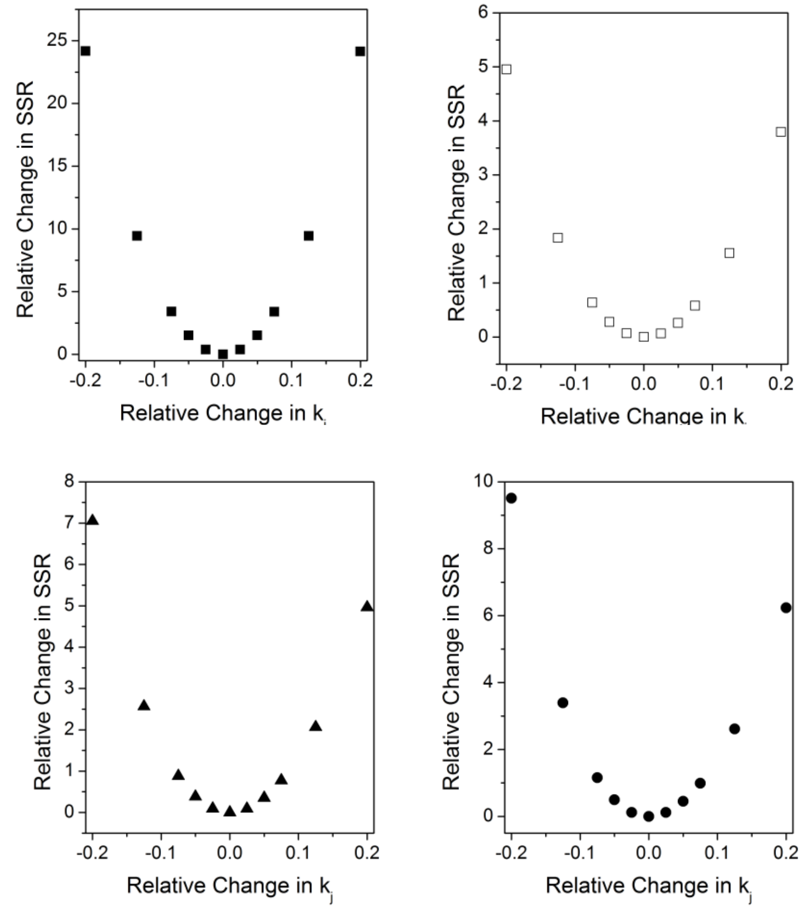

Figure S.3-2: Relative change in the sum of squared residuals (SSR) as a function of relative change (δ/k_j) in the optimal values (listed in Table 2) of the fitted rate (k_j) parameter for α (■), β (□), γ (▲), and η (●) on Pt/SiO_2.

As discussed in Section 3.3, rates on Pt/SiO_2 increased sublinearly with H_2 pressure (Fig. 9), indicative of significant coverages by one or more intermediates that contain H-atoms derived from H_2. Plausible surface intermediates that depend on H_2 include (H*) and (MHT*), which exhibit $(H_2)^{0.5}$ and $(T)(H_2)^{0.5}$ dependences, following the equilibrated steps 1.i and 1.vii (Scheme 1), respectively. The regression indicated that a given pair: (H*) and (T*), (H*) and (MHT*), or (MHT*) and (T*), could reasonably account for the kinetic behaviors observed, but the regression could not fit all three simultaneously. Deviations from first-order H_2 dependences should become more pronounced with increasing thiophene pressure (at constant H_2S/H_2), if (MHT*) were prevalent over (T*), i.e., the functional form of a rate equation that involves (H*), (MHT*), and (T*):

$$\frac{r_{Pt}}{[L]} = \frac{\alpha(H_2)(T)}{(1 \;+\; \beta(H_2)^{0.5} \;+\; \gamma(T) \;+\; \epsilon(T)(H_2)^{0.5} \;+\; \eta(H_2S)/(H_2))^2}$$

(S.3-5)

becomes

$$\frac{r_{Pt}}{[L]} = \frac{\alpha(H_2)(T)}{\left(constant \;+\; \left(\beta + \epsilon(T)\right) \cdot (H_2)^{0.5} \;+\; \gamma(T)\right)^2}$$

(S.3-6)

at constant H_2S/H_2 ratios. Measured data, however, indicated that rate dependences on H_2 approached first-order as thiophene pressure increased from 2.5 to 10 kPa (Fig. 9), implying the prevalence of (T*) and (H*) as the H_2-derived surface species.

Other H_2S-derived species on the working surface were examined by regression of measured data to functional equations that included $\theta(H_2S)$ (i.e., H_2S*) and $\zeta(H_2S)/(H_2)^{0.5}$ (i.e., HS*) as denominator terms; sensitivity analysis suggested their irrelevance in describing rates, as ∂(Relative Change in SSR)/∂(Relative Change in k_y) < 1 (where $k_y = \theta, \zeta$), indicating that H_2S* and HS* are not abundant surface species.

S.4 Chow test (F-statistic) and model discrimination

The parity between measured rates and those predicted from the rate equations (Eqs. 11 and 12) for Ru and Pt (using the optimal parameter values reported in Table 2) implies (Fig. 12) that their respective kinetic models provide accurate kinetic descriptions. The prevalence (and measurement) of empty sites (*), however, can be furthered confirmed by assessing the errors that arise from data regression to rate equations that exclude the “1” term in the denominator and that consequently contain one fewer degrees of freedom:

$$\frac{r_{Ru}}{[L]} = \frac{(H_2)(T)}{(B(T) \; + \; C(H_2S)/(H_2))^2} \tag{S.4-1}$$

$$\frac{r_{Pt}}{[L]} = \frac{(H_2)(T)}{(A(H_2)^{0.5} \; + \; B(T) \; + \; C(H_2S)/(H_2))^2} \tag{S.4-2}$$

The resulting fit is visually worse (Fig. S.4-1), consistent with greater sums of squared residuals (SSR) (Table S.4-1) for both Ru and Pt.

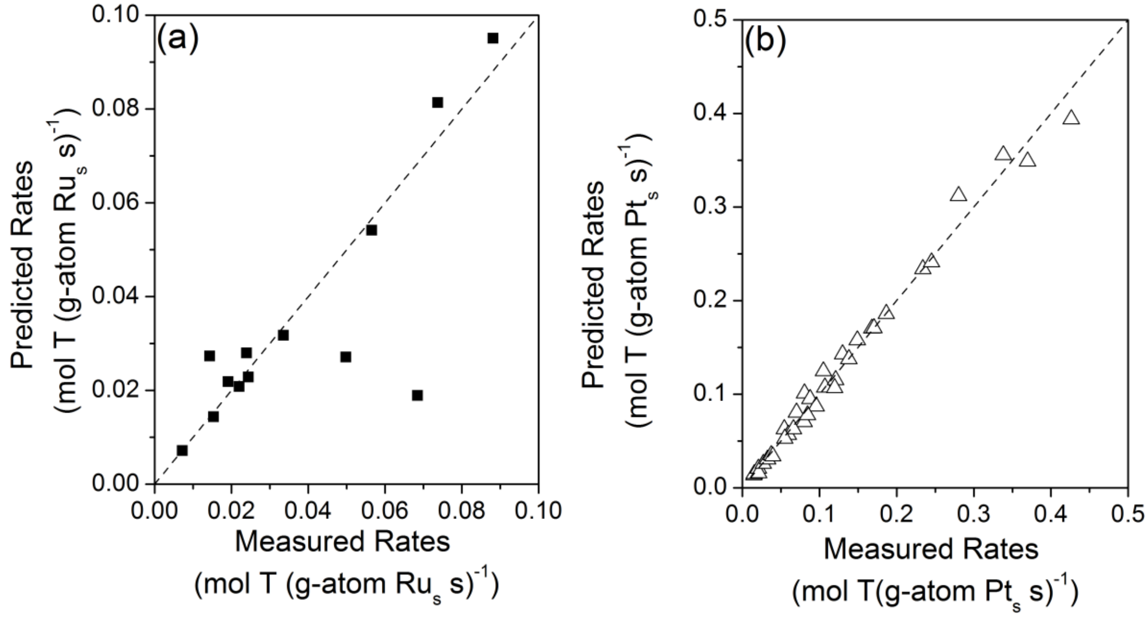

Figure S.4-1: Parity plot of measured rates and predicted rates from the rate expression for thiophene conversion on (a) Ru/SiO$_2$ (Eq. S.4-1) at 623 K and on (b) Pt/SiO$_2$ (Eq. S.4-2) at 573 K for a range of thiophene (1-10 kPa), H$_2$ (1-3 MPa) and inlet H$_2$S (0.2-10 kPa) pressures. The dashed line shown has a slope of unity.

Table S.4-1: Sum of squared residuals upon data regression to Equations S.4-1 and S.4-2 and model discrimination via Chow test.

		Ru	**Pt**
Sum of squared residuals (Eq. 11 or 12)	(SSR$_2$)	4.9×10^{-5}	1.5×10^{-3}
Degrees of freedom (Eq. 11 or 12)	(p$_2$)	3	4
Sum of squared residuals (Eq. S.4-1 or Eq. S.4-2)	(SSR$_1$)	3.3×10^{-3}	4.6×10^{-3}
Degrees of freedom (Eq. S.4-1 or Eq. S.4-2)	(p$_1$)	2	3
n (data points)		13	34
F-statistic (i.e., F; Eq. S.4-3)		659	64

Whether these increases in error arise simply from a model containing one fewer degree of freedom or from a less accurate model can be determined by the Chow test, which indicates whether the null hypothesis can be rejected on the basis of whether the associated F-statistic (F; Eq. S.4-3) exceeds that of the probable value from a statistical F-distribution.

$$F = \frac{(SSR_1 - SSR_2)/(p_2 - p_1)}{(SSR_2)/(n - p_2)}$$

(S.4-3)

According to the F-distribution, the null hypothesis can be rejected when the F-statistic exceeds 9.6 and 6.6 ($p<0.05$) or 30.8 and 16.7 ($p<0.01$) for Ru and Pt, respectively. The F-statistic values for Ru and Pt (659 and 64, respectively) indicate that the null hypothesis can be rejected and thus imply that the rate equations with greater degrees of freedom (i.e., Eqs. 11 and 12) provide a more accurate description of measured rates.

S.5 Parameter perturbation to confirm lack of cross-correlation between numerator and denominator parameters

The presence of any co-variances between numerator and denominator terms can be assessed by evaluating the change in the sum of squared residuals (SSR), as the numerator and denominator terms are simultaneously perturbed, relative to the SSR at the optimal regressed parameter values. Elongated surfaces (or contours) shaped by these errors, along the zero axes, suggest independence while intermediate slopes suggest cross correlations.

The most dominant term in the denominator is $\eta(H_2S)/(H_2)$, over the range of experimental conditions studied on Ru and Pt, and thus, any co-variance between the numerator and denominator parameters should arise from probing for cross-correlations between α and η coefficients (Eq. S.5-1).

$$\frac{r}{[L]} = \frac{\alpha(H_2)(T)}{(1 + \beta(H_2)^{0.5} + \gamma(T) + \eta(H_2S)/(H_2))^2} \tag{S.5-1}$$

As indicated by the contour plots (Fig. S.5-1) and surface projections (Fig. S.5-2) of $(SSR)_{perturbed}/(SSR)_{optimal}$ as α and η^2 are varied ±20%; weak correlations exist between these numerator and denominator parameters; furthermore, the observed behaviors reveal that errors are more sensitive to values of α than η.

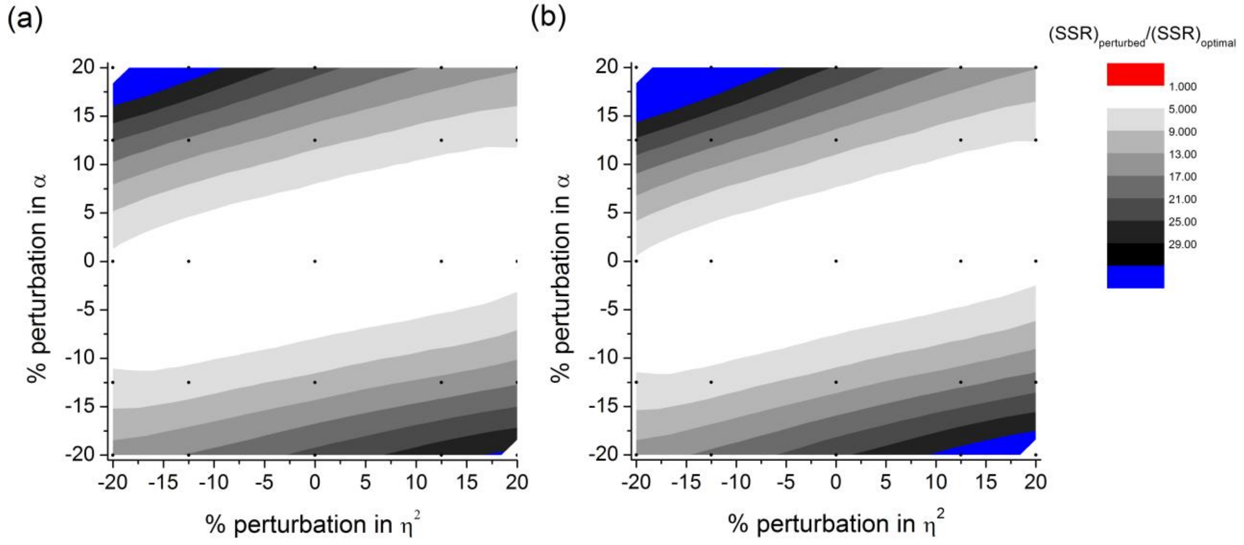

Figure S.5-1: Ratio of sum of squared residuals (SSR) upon perturbation of α and η^2 by ±20% relative to SSR at the optimal values of α and η obtained from regression of (a) Ru and (b) Pt kinetic data to Equations 11 and 12, respectively.

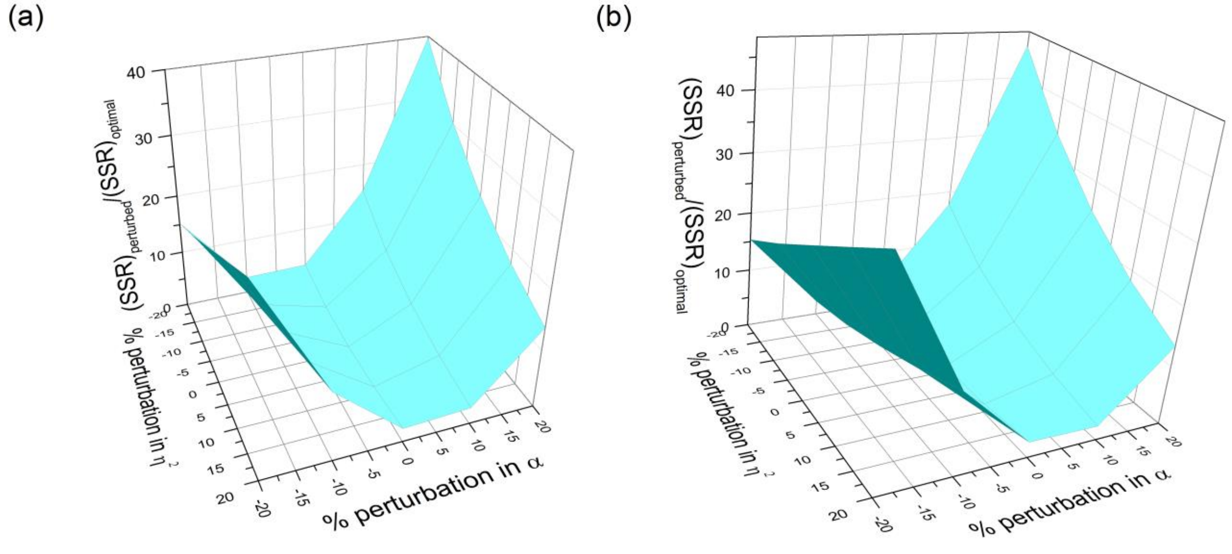

Figure S.5-2: Ratio of sum of squared residuals (SSR) upon perturbation of α and η^2 by ±20% relative to SSR at the optimal values of α and η obtained from regression of (a) Ru and (b) Pt kinetic data to Equations 11 and 12, respectively.

S.6 Deriving the expression for tetrahydrothiophene (THT) selectivity as a function of thiophene conversion (X)

The prevalent THT concentrations reflect the difference between its rate of formation (from I*, Eq. 14) and consumption (to form C_4, Eq. 16) in a plug-flow reactor at each residence time (τ):

$$\frac{d(THT)}{d\tau} = r_1 - r_3 = k_1 \cdot (H_2)^{\frac{w}{2}}(I\,*) \cdot \frac{(*)}{[L]} - k_3 \cdot (H_2)^{\frac{z}{2}}(THT) \cdot \frac{(*)^2}{[L]} \tag{S.6-1}$$

The concentration of gaseous C_4 is then given by:

$$\frac{d(C_4)}{d\tau} = r_2 + r_3 = k_2 \cdot (H_2)^{\frac{y}{2}}(I\,*) \cdot \frac{(*)}{[L]} + k_3 \cdot (H_2)^{\frac{z}{2}}(THT) \cdot \frac{(*)^2}{[L]} \tag{S.6-2}$$

This equation accounts for the rate of C_4 formation from I* via primary routes (Eq. 15) and from THT via secondary routes (Eq. 16). These two equations are solved using I* concentrations set by its pseudo-steady state through Equations 8, 14, and 15, where the rate of formation of I* equals the rate of its consumption, at any point in the reactor:

$$r - \left[k_1 \cdot (H_2)^{\frac{w}{2}} \cdot \frac{(*)}{[L]} + k_2 \cdot (H_2)^{\frac{y}{2}} \cdot \frac{(*)}{[L]}\right] \cdot (I\,*) = 0 \quad , \tag{S.6-3}$$

where r represents the total rate of thiophene conversion, which is limited by the addition of H* to MHT* (step 1.vi; Scheme 1).:

$$r = k_0^{'}(H\,*) \cdot \frac{(MHT\,*)}{[L]} = k_0 K_{H_2}(H_2) K_T K_{MHT}(T) \cdot \frac{(*)^2}{[L]} \quad , \tag{S.6-4}$$

so that the concentration of I* is defined:

$$(I\,*) = \frac{k_0 K_{H_2}(H_2) K_T K_{MHT}(T)\cdot(*)}{k_1\cdot(H_2)^{\frac{w}{2}} + k_2\cdot(H_2)^{\frac{y}{2}}} \quad , \qquad \text{(S.6-5)}$$

leading to:

$$\frac{d(THT)}{d\tau} + k_3(H_2)^{\frac{z}{2}}(THT)\cdot\frac{(*)^2}{[L]} = \frac{k_1(H_2)^{\frac{w}{2}}}{k_1\cdot(H_2)^{\frac{w}{2}} + k_2\cdot(H_2)^{\frac{y}{2}}}\cdot k_0 K_{H_2}(H_2) K_T K_{MHT}(T)\cdot\frac{(*)^2}{[L]} \qquad \text{(S.6-6)}$$

Thiophene concentration is set by the rate of its conversion (Eq. 11 or 12), and written as

$$\frac{d(T)}{d\tau} = k_0 K_{H_2}(H_2) K_T K_{MHT}(T)\cdot\frac{(*)^2}{[L]} \qquad \text{(S.6-7)}$$

Solving Equation S.6-6, with initial condition, $(T)_{\tau=0} = (T)_0$, leads to:

$$(T) = (T)_0\exp\left(-k_0 K_{H_2}(H_2) K_T K_{MHT}\cdot\frac{(*)^2}{[L]}\cdot\tau\right) \qquad \text{(S.6-8)}$$

Solving Equation S.6-6, with initial condition $(THT)_{\tau=0} = 0$, upon substituting Equation S.6-8 for (T), yields the following solution:

$$(THT) = \frac{k_1(H_2)^{\frac{w}{2}}}{k_1(H_2)^{\frac{w}{2}} + k_2(H_2)^{\frac{y}{2}}}\cdot\left(\frac{k_3(H_2)^{\frac{z}{2}}}{k_0 K_{H_2}(H_2) K_T K_{MHT}} - 1\right)^{-1}\cdot(T)_0 \cdot\left\{\exp\left(-k_0 K_{H_2}(H_2) K_T K_{MHT}\cdot\frac{(*)^2}{[L]}\cdot\tau\right) - \exp\left(-k_3(H_2)^{\frac{z}{2}}\cdot\frac{(*)^2}{[L]}\cdot\tau\right)\right\} \quad , \qquad \text{(S.6-9)}$$

which defines the concentration of THT as a function of residence time. Residence time is related to the thiophene conversion at differential conditions (X<<1):

$$(1-X)=\exp\left(-k_0 K_{H_2}(H_2)K_T\cdot\frac{(*)^2}{[L]}\cdot\tau\right) \quad , \quad , \qquad \text{(S.6-10)}$$

THT selectivity is defined as the mole of THT formed per mole of thiophene converted:

$$S_{THT}=\frac{(THT)}{(T)_0\cdot X} \quad , \qquad \text{(S.6-11)}$$

leading to the following description of THT selectivity, as a function of X, (Eq. 17):

$$S_{THT}=\frac{k_1(H_2)^{\frac{w}{2}}}{k_1(H_2)^{\frac{w}{2}}+k_2(H_2)^{\frac{y}{2}}}\cdot\left(\frac{k_3(H_2)^{\frac{z}{2}}}{k_0K_{H_2}(H_2)K_TK_{MHT}}-1\right)^{-1}\cdot\frac{\left\{(1-X)-(1-X)^{\frac{k_3(H_2)^{\frac{z}{2}}}{k_0K_{H_2}(H_2)K_TK_{MHT}}}\right\}}{X} \qquad \text{(S.6-12)}$$

The linear form of the THT selectivity equation (Eq. 21) can be obtained by first applying a second-order Taylor series on THT concentration (Eqs. S.6-9 and S.6-10), about X=0:

$$(THT)=\frac{k_1(H_2)^{\frac{w}{2}}}{k_1(H_2)^{\frac{w}{2}}+k_2(H_2)^{\frac{y}{2}}}\cdot\left(\frac{k_3(H_2)^{\frac{z}{2}}}{k_0K_{H_2}(H_2)K_TK_{MHT}}-1\right)^{-1}\cdot(T)_0\cdot\left\{\frac{d}{dX}\left[(1-X)-(1-X)^{\frac{k_3(H_2)^{\frac{z}{2}}}{k_0K_{H_2}(H_2)K_TK_{MHT}}}\right]_{X=0}(X)+\frac{1}{2}\frac{d^2}{dX^2}\left[(1-X)-(1-X)^{\frac{k_3(H_2)^{\frac{z}{2}}}{k_0K_{H_2}(H_2)K_TK_{MHT}}}\right]_{X=0}(X)^2\right\} \qquad \text{(S.6-13a)}$$

$$= \frac{k_1(H_2)^{\frac{w}{2}}}{k_1(H_2)^{\frac{w}{2}} + k_2(H_2)^{\frac{y}{2}}} \cdot \left(\frac{k_3(H_2)^{\frac{z}{2}}}{k_0 K_{H_2}(H_2) K_T K_{MHT}} - 1\right)^{-1} \cdot (T)_0$$

$$\cdot \left\{\left[\frac{k_3(H_2)^{\frac{z}{2}}}{k_0 K_{H_2}(H_2) K_T K_{MHT}} - 1\right](X) + \frac{1}{2}\left[(-1) \cdot \frac{k_3(H_2)^{\frac{z}{2}}}{k_0 K_{H_2}(H_2) K_T K_{MHT}} \cdot \left(\frac{k_3(H_2)^{\frac{z}{2}}}{k_0 K_{H_2}(H_2) K_T K_{MHT}} - 1\right)\right](X)^2\right\}$$

(S.6-13b)

$$= \frac{k_1(H_2)^{\frac{w}{2}}}{k_1(H_2)^{\frac{w}{2}} + k_2(H_2)^{\frac{y}{2}}} \cdot (T)_0 \left\{(X) - \frac{1}{2}\left[\frac{k_3(H_2)^{\frac{z}{2}}}{k_0 K_{H_2}(H_2) K_T K_{MHT}}\right](X)^2\right\}$$

(S.6-13c)

This form of THT concentration (Eq. S.6-13c) is then substituted into Equation S.6-11 to obtain the linearized THT selectivity function:

$$S_{THT} = \frac{k_1(H_2)^{\frac{w}{2}}}{k_1(H_2)^{\frac{w}{2}} + k_2(H_2)^{\frac{y}{2}}} \cdot \left\{1 - \frac{1}{2}\left[\frac{k_3(H_2)^{\frac{z}{2}}}{k_0 K_{H_2}(H_2) K_T K_{MHT}}\right] X\right\}$$

(S.6-14)

S.7 Butane to butene ratio as a function of total C_4 selectivity

Secondary hydrogenation reactions that saturate butene ($C_4^=$) to form butane (C_4^0) products also occur on the interstices within the refractory templates formed on the surfaces of Ru, Pt, Re, and ReS_x. $C_4^0/C_4^=$ ratios increase with C_4 selectivity but their values (<2.5) are significantly lower than those expected from equilibrated linear alkane-alkene interconversions (~10^5-10^6 at 1-3 MPa H_2, 573-623 K), expected on bare metal surfaces at similar conditions; such observations further substantiate the notion that these interstitial spaces compose a passivated surface that binds adsorbates, intermediates, and transition states more weakly than their respective bare metal surface.

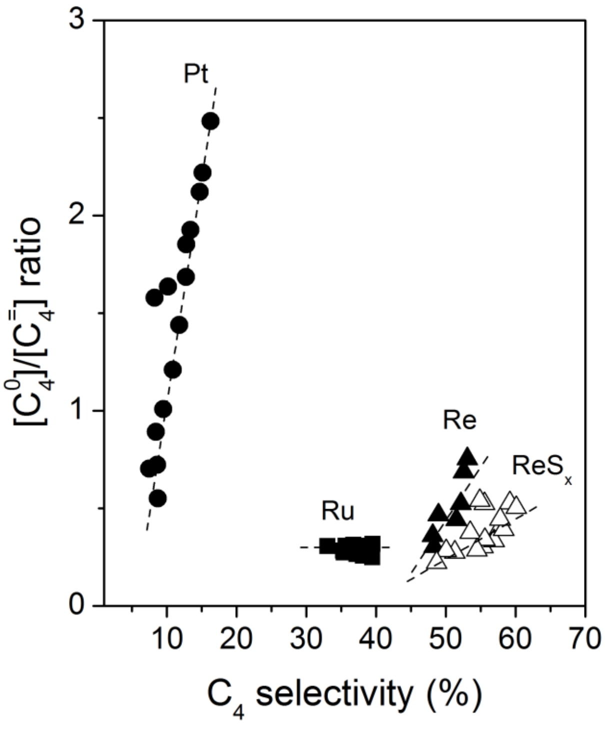

Figure S.7-1: Butane (C_4^0)/butene ($C_4^=$) molar ratios as a function of C_4 (butane + butene) selectivity at 2.0 MPa H_2, 2.5 kPa thiophene, on Ru/SiO_2 (■) at 623 K and 6.7-50. × 10^{-4} inlet H_2S/H_2, Pt/SiO_2 (●) at 573 K and 1-10. × 10^{-4} inlet H_2S/H_2, Re/SiO_2 (▲) at 573 K and 0.7-5 × 10^{-4} inlet H_2S/H_2, and ReS_x/SiO_2 (△) at 573 K and 1.7-5 × 10^{-4} inlet H_2S/H_2. Dashed lines indicate trends.